Available online at www.sciencedirect.com

ScienceDirect

International Journal of Multiphase Flow 34 (2008) 1175–1184

International Journal of Multiphase Flow

www.elsevier.com/locate/ijmulflow

Multi-channel effect of condensation flow in a micro triple-channel condenser

Wei Zhang [a,b], Jinliang Xu [a,*], Guohua Liu [a,b]

[a] Micro Energy System Laboratory, Key Laboratory of Renewable Energy and Gas Hydrate, Guangzhou Institute of Energy Conversion, Chinese Academy of Sciences, Wushan, Nengyuan Road, Guangzhou, Guangdong 510640, PR China
[b] Graduate University of Chinese Academy of Sciences, Beijing 100039, PR China

Received 10 April 2008; received in revised form 27 May 2008
Available online 12 June 2008

Abstract

Multi-channel effect is important to understand transport phenomenon in phase change systems with parallel channels. In this paper, visualization studies were performed to study the multi-channel effect in a silicon triple-channel condenser with an aspect ratio of 0.04. Saturated water vapor was pumped into the microcondenser, which was horizontally positioned. The condenser was cooled by the air natural convention heat transfer in the air environment. Flow patterns are either the annular flow at high inlet vapor pressures, or a quasi-stable elongated bubble at the microchannel upstream followed by a detaching or detached miniature bubble at smaller inlet vapor pressures. The downstream miniature bubble was detached from the elongated bubble tip induced by the maximum Weber number there.

It is observed that either a single vapor thread or dual vapor threads are at the front of the elongated bubble. A miniature bubble is fully formed by breaking up the vapor thread or threads. The transient vapor thread formation and breakup process is exactly symmetry against the centerline of the center channel. In side channels, the Marangoni effect induced by the small temperature variation over the channel width direction causes the vapor thread formation and breakup process deviating from the side channel centerline and approaching the center channel. The Marangoni effect further forces the detached bubble to rotate and approach the center channel, because the center channel always has higher temperatures, indicating the multi-channel effect.

Keywords: Condensation; Multi-channel effect; Flow pattern; Microchannel; Marangoni effect

1. Introduction

Condensation in macrochannels has been studied for nearly one century and is well understood, involving many engineering applications. Recently, miniaturization of systems brings new challenges and opportunities on the condensation flow and heat transfer. Principles of condensation in macrochannels may not be directly applied in microsystems, due to the possible size effect. In contrast to the widely studied microscale boiling heat transfer, condensation in microchannels is not well understood and needs further investigation.

Baird et al. (2003) developed a novel experimental apparatus allowing for a quantitative control of local heat transfer to fine passages through thermoelectric cooler. Local heat transfer coefficients were obtained for condensation flow of HCFC-123 and R11 in tubes with inner diameters of 0.92 and 1.95 mm. It is concluded that the tube diameter had little effect on the local heat transfer coefficients. Médéric et al. (2005) visualized the condensation flow pattern in a capillary tube with the inner diameter of 0.56 mm and a length of 100 mm. Tests were performed using *n*-pentane as the working fluid at constant mass fluxes in the range of 0–18 $\mathrm{kg/m^2\,s}$. The transient and time-averaged void fractions along the axial position were obtained by analyzing the digital photographs. Shin and Kim (2004) measured local condensation heat transfer coefficients in sub-millimeter channels. Using

---

[*] Corresponding author. Tel./fax: +86 20 87057656.
E-mail address: xujl@ms.giec.ac.cn (J. Xu).

0301-9322/$ - see front matter © 2008 Elsevier Ltd. All rights reserved.
doi:10.1016/j.ijmultiphaseflow.2008.05.004

R134a as the working fluid, the pressure drop and heat transfer coefficient were investigated. Médéric et al. (2004) studied flow patterns in tubes with three diameters of 10.0, 1.1 and 0.56 mm. Flow patterns are divided into three types: the annular flow, the Taylor-bubble flow and the isolated spherical collapsing bubble flow. Wang et al. (2004) proposed a theoretical model to compute the film condensation heat transfer coefficient in square cross-section horizontal minichannels. Effects of surface tension, vapor shear stress and gravity were taken into account to perform simulations with R134a as the working fluid in a 1.0 mm diameter channel. In a separate paper by Wang and Rose (2006), the theoretical model was further verified for the film condensation heat transfer in microchannels. Garimella et al. (2002, 2005) proposed a semi-empirical model for pressure drops with intermittent condensation flow of refrigerant R134a in horizontal minichannels. The hydraulic diameters considered are in the ranging of 0.5–4.91 mm. Bandhauer et al. (2006) developed a model to evaluate the condensation heat transfer in circular microchannels and compared their results with measured values. Coleman and Garimella (2002) experimentally studied the condensation flow mechanism in capillaries with different cross-sectional geometries. Four flow patterns including intermittent flow, wavy flow, annular flow and dispersed flow were identified. It is observed that the geometry and aspect ratio of the capillaries have less effect on the flow pattern transitions. Kalman (2003, 2006) visualized the shrinking bubble by condensation in miscible and immiscible liquids. The boundary layer model and the envelop model were developed. Louahlia-Gualous and Mecheri (2007) experimentally studied steam condensation in a single miniature tube. By varying the inlet pressures and cooling rates, the annular, slug bubble flow, spherical bubbly flow and wavy flow were observed.

The above cited references concern the condensation flow in glass or metallic channels. Microcondensers fabricated with MEMS technology ensure good comparability with electronic systems. Thus silicon based condenser is attracting many scientists and engineers. Wu and Cheng (2005) studied flow patterns in microchannels with trapezoid cross-section. The microchannels were fabricated in a silicon wafer bonded with a Pyrex glass cover, allowing for flow visualizations. Pure water steam was used as the working fluid. The silicon wafer was cooled by attaching a heat sink inside which the 8 °C cold water was flowing through. Various flow patterns, such as fully droplet flow, droplet/annular/injection/slug-bubbly flow, annular/injection/slug-droplet flow and fully slug-bubbly flow, were observed in their study. Hu and Chao (2007) visualized flow patterns during condensation of water steam in silicon microchannels with the trapezoid cross-section. The etched microchannels had a hydraulic diameter in the range of 73–237 μm. Five different flow patterns were observed and the slug-bubbly flow was found to be the dominant flow pattern, determining the heat transfer and pressure drop in the microcondenser.

In a previous paper by Zhang et al. (2008), we found the periodic bubble emission and appearance of an ordered bubble train during condensation of saturated water steam in a *single* silicon microchannel. Effects of cooling rates and mass fluxes on the bubble emission frequency were studied. It is found that the size and bubble emission frequency could be controlled precisely by varying the cooling rates and inlet steam pressures. Such a study provides a new method for miniature bubble generation for microfluidic applications. The present work is the extension of such a study, focusing on the *multi-channel effect* of condensation flow in triple microchannels. To the authors' knowledge, no studies examined the detailed multi-channel effect for the phase change heat transfer in micron scale.

2. Experiment

2.1. Design of the microcondenser

Usually deep microchannels have sufficiently large surface to volume ratio, which is recommended to be used in microscale heat transfer devices. However, deep microchannels induce difficulties for the flow visualization studies. Thus in the present study, we rotate the deep microchannels by 90°, forming the shallow but wider microchannels. In terms of this, the bubble shape, size, generation frequency can be easily visualized and recorded by a high speed camera.

Fig. 1a shows the three-dimensional microcondenser, fabricated by the Microelectromechanical systems (MEMS) technology. The chip is a silicon wafer with a thickness of 400 μm bonded with a 7740 Pyrex glass cover, allowing for flow visualizations of the microflow. Along the flow direction, three successive zones were etched: the inlet vapor plenum, the three parallel microchannels, and the outlet fluid plenum. Fig. 1b and c show the top view of the silicon wafer and the cross-section of the microchannels in the central part, respectively. Both the inlet and outlet fluid plenums have the rectangular cross-section with the depth of 120 μm and width of 3000 μm. Each microchannel has a length of 5000 μm with the cross-section of 30 μm depth and 800 μm width. The fin width between two neighboring microchannels is 50 μm, forming the whole width of the microchannel area of 2500 μm. The chip has an entire width of 5000 μm. A three-dimensional coordinate system was attached on the wafer at the entrance of the three microchannels. The original point is arranged at the center of the three microchannels, as seen in Fig. 1a and b. The axial coordinate refers to the flow direction while the y-coordinate is the channel width direction. The z-coordinate is perpendicular to the wafer plane and its original point starts from the bottom of the microchannels. Channel 2 is the center microchannel, while channels 1 and 3 are the two side channels, which are symmetrically arranged against the center channel 2.

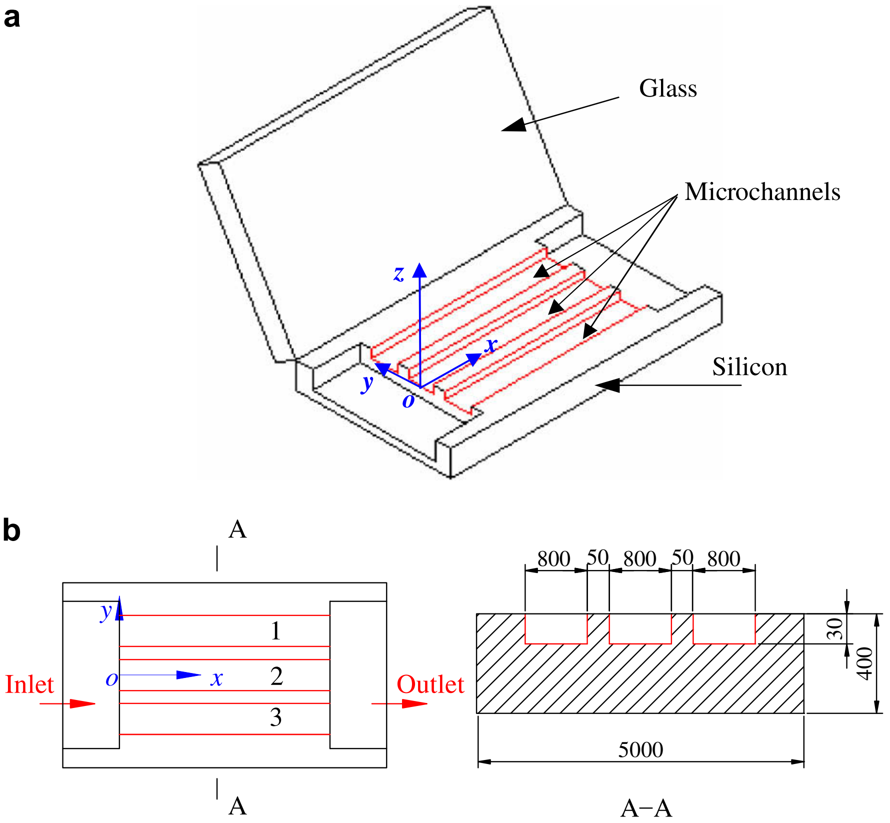

Fig. 1. The microcondenser used in the present study (all dimensions in μm).

2.2. Experimental facility

Fig. 2 shows the experimental test loop, consisting of four subsystems: the pressure and temperature controlled steam generator, the micro condenser test section, the microscope and high speed camera, and the electronic balance for the flow rate measurement of the condensed liquid flow rate.

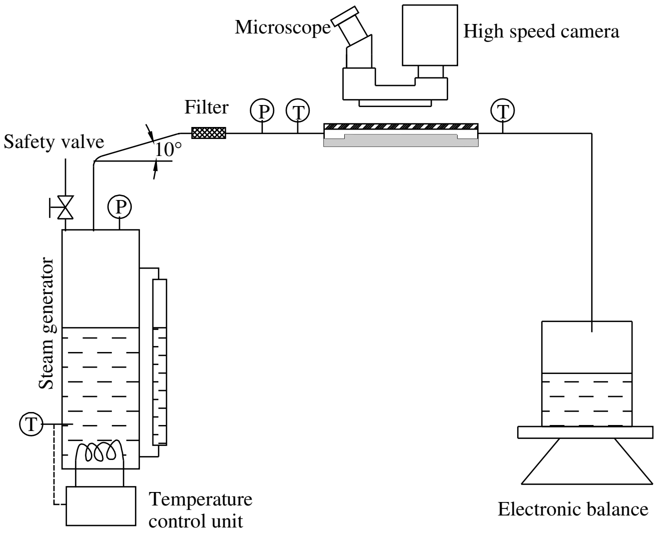

Fig. 2. Experimental setup.

A soft capillary tube connects the steam generator and the micro condenser. Along the flow path of the test loop, a 2 μm filter, a pressure transducer and a miniature thermocouple were installed successively. The vapor temperature at the microchannel inlet was measured by a K-type thermocouple located as close to the micro condenser as possible. A carefully designed miniature adapter connects the capillary tube and the micro condenser. To prevent the vapor condensation before entering the silicon chip, a small diameter metallic wire was wrapped at the outer surface of the capillary tube and used as a heater, driven by an adjustable AC power supply. The capillary tube was further wrapped with a thermally insulating material.

To operate the system, initially degassed and deionized water was stored in the steam generator which had an electric heater at its bottom. Power was supplied to the heater to boil the water. Fluid pressure and temperature in the steam generator was well controlled. A high precision pressure transducer and a safety valve were installed at the top of the steam generator. The safety valve was set at the desired pressure value for operation. When the desired pressure was reached in the steam generator, the safety valve automatically discharged vapor through an auxiliary capillary tube to a cold liquid pool (not shown in Fig. 2). Initially the discharged vapor contains the air content. The discharged vapor is rapidly condensed by the subcooled liquid while the air is released to the environment. The discharge process is stopped until no any air bubbles come out of the liquid pool. Thus the water in the steam generator is completely degassed, verified also by the fact that the vapor pressure and temperature in the steam generator correspond with each other at the saturation state. For this, the liquid temperature was monitored by a K-type jacketed thermocouple which is installed on the side wall of the steam generator tank (see Fig. 2). In this way, only pure saturated water vapor without any non-condensable gas enters the inlet plenum of the micro condenser.

The micro condenser chip was directly exposed in the air environment. The laboratory temperature was well controlled by an air-conditioning system at 20 °C with the uncertainty of 1 °C. In order to stabilize the natural convection heat transfer between the silicon chip and the air environment, the bottom part of the silicon chip is contained in a larger glass beaker, preventing the air flow disturbance.

Because the mass flow rate of the micro condenser is small, typically on the order of nanoliters per second, the water vapor mixture is completely condensed in the capillary tube downstream of the micro condenser, which is exposed in the air environment. The fully condensed water is collected in a small beaker and the mass is weighed with an electronic balance of high precision to determine the flow rate.

2.3. Instrumentation, measurements and uncertainties

K-type jacketed thermocouples measured the inlet and outlet fluid temperatures, T_{in} and T_{out}, having accuracies of 0.3 °C. The inlet pressure is measured by a Senex pressure transducer with an accuracy of 0.1% FS. The liquid mass measurement has the uncertainty of 0.02 g. The outlet pressure of the micro condenser equals to the atmospheric pressure, due to the fact that the cross-sectional area of the connected capillary tube downstream of the micro condenser is two orders larger than that of the micro condenser. The pressure drop downstream of the micro condenser can be neglected. The response time is either 0.01 s for the pressure transducer or 0.1 s for the 0.2 mm diameter thermocouples. The pressure and temperature signals were recorded by a high speed data acquisition system (DL 750, Yokogawa, Inc., Japan) with 16 channels. The data sampling rates can reach 10 million samples per second with this system. In the present study the recording rate is selected as 100 samples per second, which is fast enough to catch the response time of the pressure and temperature signals.

A high speed camera incorporating a stereo microscope allows for the flow visualization of the microflow. The microscope is a Leica M stereo microscope (Germany). The high speed camera is an X-stream Vision Xs-4 (IDT Inc., USA) which has a recording rate up to 5130 frames per second with the maximum resolution of 512 × 512 pixels. In this study, recording rates of 4000–5000 frames per second and a resolution of 512 × 512 pixels were used, which was sufficient for the transient flow pattern observations. The field of view for condensation in the microchannel had an area of 5000 μm × 3000 μm corresponding to a resolution of 433 × 250 pixels, leading to an uncertainty of 11 μm for the bubble dynamics measurement.

2.4. Test conditions

Experimental parameters covered the following data ranges: inlet pressures from 123.12 to 215.36 kPa, inlet temperatures from 105.6 to 122.6 °C and mass fluxes from 109.14 to 228.58 kg/m^2 s. Mass fluxes were computed by the mass flow rate divided by the three cross-section area of 3 × 800 μm × 30 μm.

In the present study, the fluid pressure and temperature were stable over time, which is not always the case for phase change heat transfer in microchannels. There are two reasons to achieve the high stability of these values: (1) transient flow patterns in the millisecond timescale do not affect the fluid states at the inlet and outlet and (2) flow visualization with the high speed camera permits much higher time resolution compared to the pressure and temperature signals. In other words, the fluid pressure and temperature signals do not identify high frequency oscillations on the order of 1000 Hz. This behavior is similar to that of Xu et al. (2006) for the microscale boiling heat transfer on the millisecond timescale.

3. Results and discussion

3.1. General flow patterns

Usually, there are two types of flow patterns in the triple microchannels shown in Fig. 3. The main flow pattern is a quasi-stable elongated bubble followed by a detaching or detached bubble (Fig. 3a and b). A previous study by Zhang et al. (2008) shows that higher cooling rates make the miniature bubbles densely populated, forming a bubble train followed by the elongated bubble. Another flow pattern observed is the annular flow when the inlet pressure of the saturated vapor is sufficiently high (Fig. 3d). Fig. 3c shows the transition from the elongated bubble plus the miniature bubble pattern to the annular flow pattern. As noted by Zhang et al. (2008) for the condensation flow in a single microchannel, cooling rate of the micro condenser strongly affects the bubble shape and size. The air natural convection heat transfer at the outer surface of the silicon chip yields larger elliptical bubbles followed by the elongated bubble.

It is known that the present microchannel geometry plays an important role for the formation of the upstream elongated bubble. The inlet plenum (see Fig. 1) is wider and deeper than the three central microchannels. The mass flux in the inlet plenum is much smaller than those in the three central microchannels with each cross-section of 800 μm × 30 μm. Due to this fact, a quasi-stable elongated bubble can be generated by the surface tension force when the vapor flows across the junction interface from the inlet

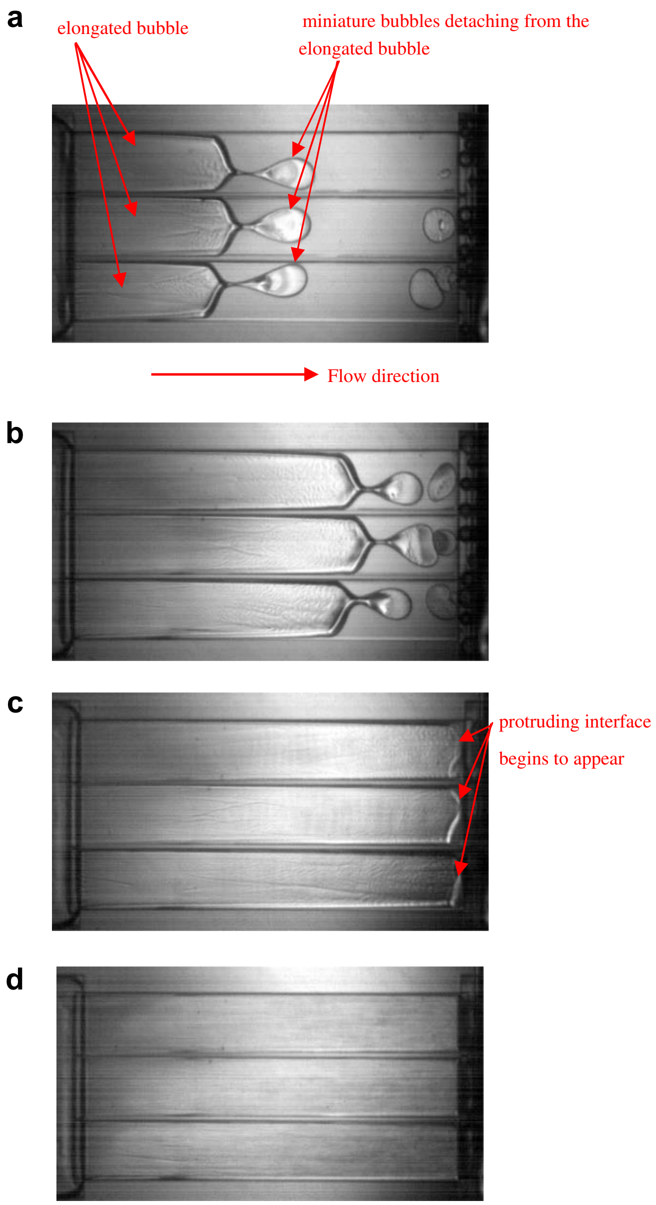

Fig. 3. Flow patterns identified in the present study at different inlet saturated pressures. (a) Upstream elongated bubbles followed by miniature detaching bubbles; (b) the longer elongated bubbles with higher inlet pressures; (c) the water vapor interface outflowing the microchannels; (d) annular flow at sufficiently high inlet pressures.

plenum to each of the three central microchannels. The inlet pressure is mainly overcome by the surface tension force due to the curvature interface of the elongated bubble.

The present study identifies multi-channel effects of condensation flow in parallel microchannels. These effects are due to the miniature temperate variations over the channel width direction, which will be described as follows.

3.2. Condensation flow in the center microchannel 2

The three central microchannels are exactly symmetrically arranged in the chip width direction, thus flow patterns in the center channel 2 (see Fig. 1) are symmetry against the centerline of the channel 2. This is verified in Figs. 4 and 5, indicating two different miniature bubble separation modes from the elongated bubble.

The single vapor thread separation mode from the elongated bubble is shown in Fig. 4 for a full cycle. A new cycle begins when a miniature bubble is fully released from the elongated bubble at $t = 1.00$ ms in Fig. 4. After that the front interface of the elongated bubble becomes protruding, and the vapor is gradually released to form a circular bubble (see images for $t > 19.00$ ms in Fig. 4). A vapor thread connects the elongated bubble and the miniature bubble at $t = 86.00$ ms, and is broken up thus a new miniature bubble is completely formed at $t = 87.00$ ms, ending the present miniature bubble generation cycle.

At the front interface of the elongated bubble, there exist an inertia force and a surface tension force. The Weber number is defined as $We = \rho_v u^2 D/\sigma$, where ρ_v is the vapor density, u is the local vapor velocity towards the vapor–liquid interface inside the elongated bubble, D is the hydraulic diameter, and σ is the surface tension force. The Weber number indicates the inertia force relative to the surface tension force, governing the bubble or droplet breakup process (Stone et al., 2004). The interface can be broken up once the Weber number is sufficiently large.

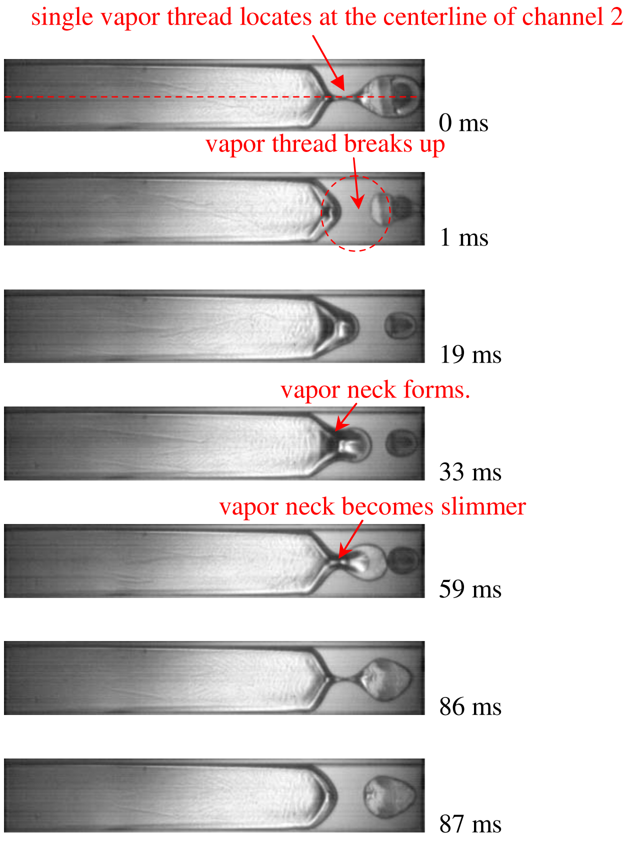

Fig. 4. Formation of miniature bubble at the front of the elongated bubble in the central channel 2, single vapor thread breakup mode ($p_{in} = 133.17$ kPa, $G = 123.6$ kg/m^2 s).

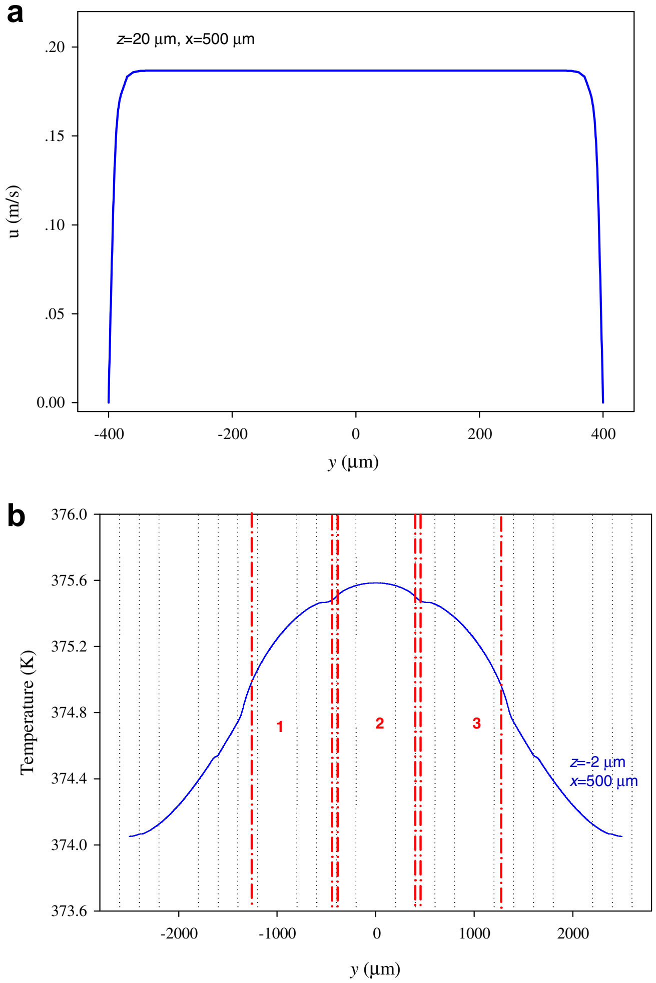

Fig. 5. Vapor velocity and silicon substrate temperature distribution across the channel width direction. (a) The vapor velocity distribution along channel width direction; (b) the temperature distribution across the channel width.

The Weber number is varied along the front interface of the elongated bubble and it gets the maximum value at the elongated bubble tip, in the center channel 2. This is because the bottom channel surface has the maximum temperature at that location, yielding a smallest surface tension force there.

For a pressure-driven fully-developed laminar flow in the rectangular microchannel, the velocity profile is computed as (Purday, 1949)

$$u = u_{\max}\left[1-\left(\frac{y}{b}\right)^{n}\right]\left[1-\left(\frac{z}{a}\right)^{m}\right] \tag{1}$$

where $u_{\max}$ is the maximum velocity at the centerline and at the half height of the center channel 2, a and b are the height and width of the rectangular channel, m, n are constant numbers depending on the channel geometry parameters of a and b.

$$m = 1.7 + 0.5(2b/2a)^{-1.4}, \quad n = \begin{cases} 2, & \frac{b}{a} \leqslant \frac{1}{3} \\ 2 + 0.3\left(\frac{b}{a} - \frac{1}{3}\right), & \frac{b}{a} \geqslant \frac{1}{3} \end{cases} \tag{2}$$

$u_{\max}$ is calculated as $u_{\max} = U\left(\frac{m+1}{m}\right)\left(\frac{n+1}{n}\right)$, where U is the average vapor velocity at the microchannel entrance.

Fig. 5a shows the vapor velocity profile at $x = 500$ µm and $z = 20$ µm for the channel 2. The velocity has a large gradient near the side wall surface and is almost uniform for the major part of the microchannel.

In order to estimate the temperature distribution over the whole etched channel surface, numerical simulation was performed using the commercial software FLUENT 6.0 package. The calculations were performed at the inlet mean vapor velocity of 0.12 m/s (mass flux of 120 kg/m^2 s). The outlet boundary condition is set as the outflow. Both the Pyrex glass cover and the etched silicon substrate were considered. The fluid flow in the etched structures is conjugated with the thermal conduction in the solid silicon. The outer surface of the whole silicon chip has the air natural convection heat transfer coefficient of 10.0 W/mK. Fig. 5b shows the temperature distribution at $x = 500$ µm below the etched bottom channel surface of 2.0 µm. It is seen that the center channel 2 has the symmetry temperature distribution with a slight higher temperature at the centerline of y=0. However, the side channels 1 and 3 have higher temperatures at the locations close to the center channel 2. This temperature distribution affects the miniature bubble generation at the front of the elongated bubble, and the movement of the miniature bubble after its departure from the elongated bubble, which will be described in Section 3.3.

The above estimation explains why the interface breakup point takes place at the centerline of the center channel 2. Once the vapor phase is released to form a bubble, the shear stress coming from the surrounding liquid flow across the bubble will breakup the vapor thread, thus a new miniature bubble is completely generated downstream of the elongated bubble.

For the same run case shown in Fig. 4, another dual vapor thread breakup mode was identified. Fig. 6 shows the transient evolution of the miniature bubble generation process. Similarly a new cycle for the new bubble generation is defined at $t = 1.00$ ms. After that the elongated bubble interface becomes protruding. In contrast to the bubble detachment mode shown in Fig. 4, the vapor phase is releasing through two points at the elongated bubble interface, forming an O-ring structure inside which liquid is contained. In front of the O-ring is a moon shape meniscus. In other words, the double curved vapor threads, which are exactly symmetry against the centerline of the center channel 2, enclose liquid. The dual vapor threads become slimmer and slimmer, finally break up and a new bubble is completely formed at $t = 31.00$ ms in Fig. 6.

In summary, flow patterns in the center channel for the multi-microchannel system is similar to those in a single microchannel, which is reported in Zhang et al. (2008). Flow images are exactly symmetry against the centerline of the microchannel. Two miniature bubble formation modes are identified. One is the single vapor thread breakup mode, the other is the dual vapor threads breakup mode.

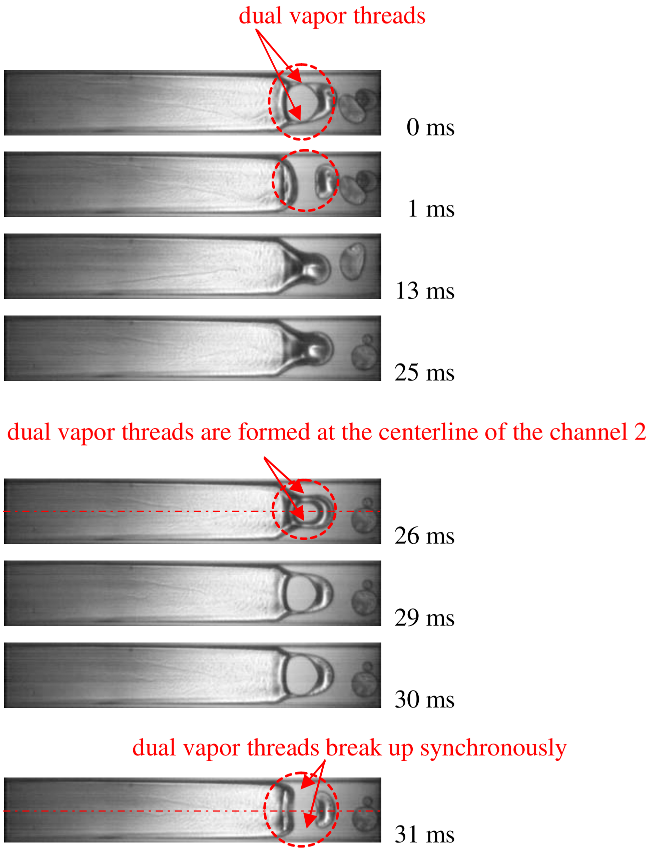

Fig. 6. Formation of miniature bubble at the front of the elongated bubble in the central channel 2, double vapor thread breakup mode ($p_{\text{in}} = 133.17\ \text{kPa}, G = 123.6\ \text{kg/m}^2\ \text{s}$).

3.3. Condensation flow in the side microchannels 1 and 3

It is found that the miniature temperature variation over the channel width direction affects the bubble formation process in the side channels 1 and 3. An example of the miniature bubble formation is shown in Fig. 7. Examining the etched channel surface temperature in the y-direction in Fig. 5b finds that the temperature is higher at the locations close to the center channel 2. Such distribution first leads to the non-symmetry elongated bubble interface. The elongated bubble interface tip deviates from the centerline of the side channel 3 and approaches the center channel 2. Besides, the elongated bubble interface tip has the larger Weber number caused by the smaller surface tension force induced by larger etched channel surface temperature there. This mechanism causes the vapor phase releasing through the interface tip to form a new miniature bubble at the front of the elongated bubble. The single vapor thread connecting the elongated bubble and the miniature bubble deviates from the centerline of the side channel 3 and approaches the center channel 2. During the miniature bubble formation process and after its complete formation, the miniature bubble is nearly contacts the side wall of the channel 3, due to a net pressure force towards the center channel 2 applied on the miniature bubble caused by the Marangoni effect. A driving force applied on a bubble toward the higher temperature region due to the Marangoni effect can be computed as $2\int_0^{\pi} \frac{\partial\sigma(T_{\text{f}})}{\partial T_{\text{f}}}\frac{\partial T_{\text{f}}}{R\partial\tilde{\theta}}\sin\tilde{\theta}\cdot R\mathrm{d}\tilde{\theta}$, where T_{f} is the liquid temperature enclosing the bubble interface, $\tilde{\theta}$ is the angle coordinate along the bubble interface, in terms of Takahashi et al. (1999).

Similar to the two miniature bubble detaching modes in the center channel 2, the dual vapor threads breakup mode for the miniature bubble formation also occurs in the side channels. An example of the dual vapor threads breakup mode is shown in Fig. 8 for the side channel 1. Again, due to the non-symmetry temperature distribution of the etched channel surface in the y-direction, the two vapor threads are not symmetry against the centerline of the channel. As shown in Fig. 8, a previous cycle is the typical single vapor thread breakup mode, which is described in Fig. 7. However, a new cycle for the dual vapor threads breakup for a new miniature bubble formation starts from $t = 0.50$ ms in Fig. 8. An O-ring structure is observed to deviate from the centerline of the channel 1 and approach the center channel 2. The vapor thread that is close to the center channel 2 breaks up first at $t = 28.75$ ms in Fig. 8, leaving another vapor thread connecting the elongated bubble and the miniature bubble. The remaining vapor thread then migrates towards the center channel 2, as marked by the arrows for $t > 30.00$ ms in Fig. 8. It is thoroughly broken up at $t = 67.00$ ms and a new bubble is completely generated. Fig. 9 shows the remaining vapor thread migrating from the lower temperature side to the higher temperature side, across the channel centerline of $y = 850\ \mu\text{m}$ at $t = 33.75$ ms.

Fig. 10 compares the miniature bubble trajectories after their fully separation from the elongated bubble in the side channel 1 and the center channel 2. It is seen that the quasi-stable elongated bubble and the detached miniature bubble are symmetrically populated in the center channel at any time. However, the non-symmetry structure was observed in the side channel 1. After the separation of the miniature bubble, two forces are applied on the miniature elliptical bubble. One is the shear force induced by the flow velocity difference between the bubble and its surrounding liquid. This force is along the flow direction. The other is the force induced by the Marangoni effect caused by the non-uniform temperature of the etched channel surface. This force always guides the bubble towards the higher temperature zone, i.e., the center channel 2. The Marangoni effect directs the miniature bubble contacting the side wall of the channel 1. The combined effect of the two forces rotates the bubble, i.e., the bubble is switched from the inclined position when it is just separated from the elongated bubble to the “standing up” state at the microchannel exit.

We compare the cycle periods of the miniature bubble generation from the elongated bubble in the center channel and the two side channels in Fig. 11, for the two selected run cases. Cycle periods for the miniature bubble

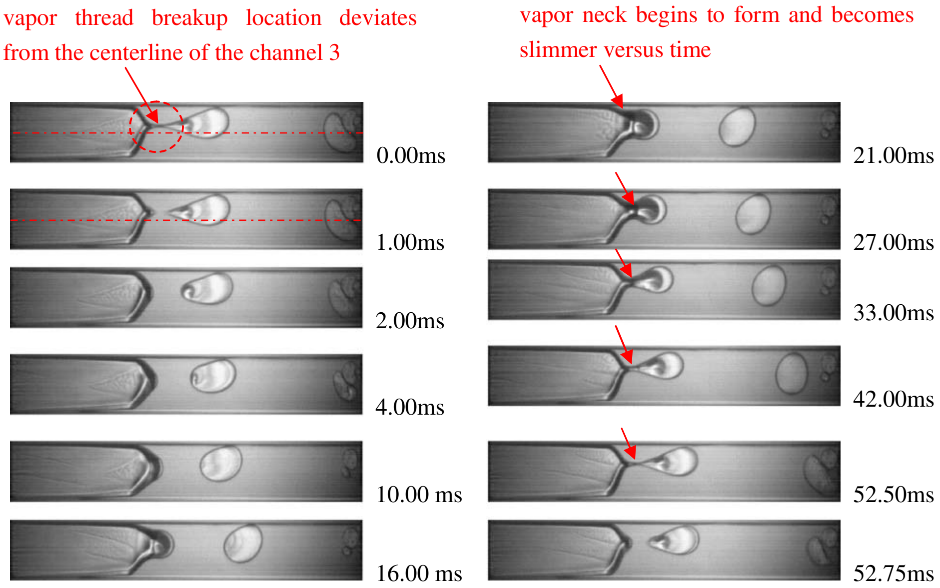

Fig. 7. Miniature bubble formation at the front of elongated bubble in the side channel 3, single vapor thread breakup mode ($p_{in} = 123.12$ kPa, $G = 109.1$ kg/m^2 s).

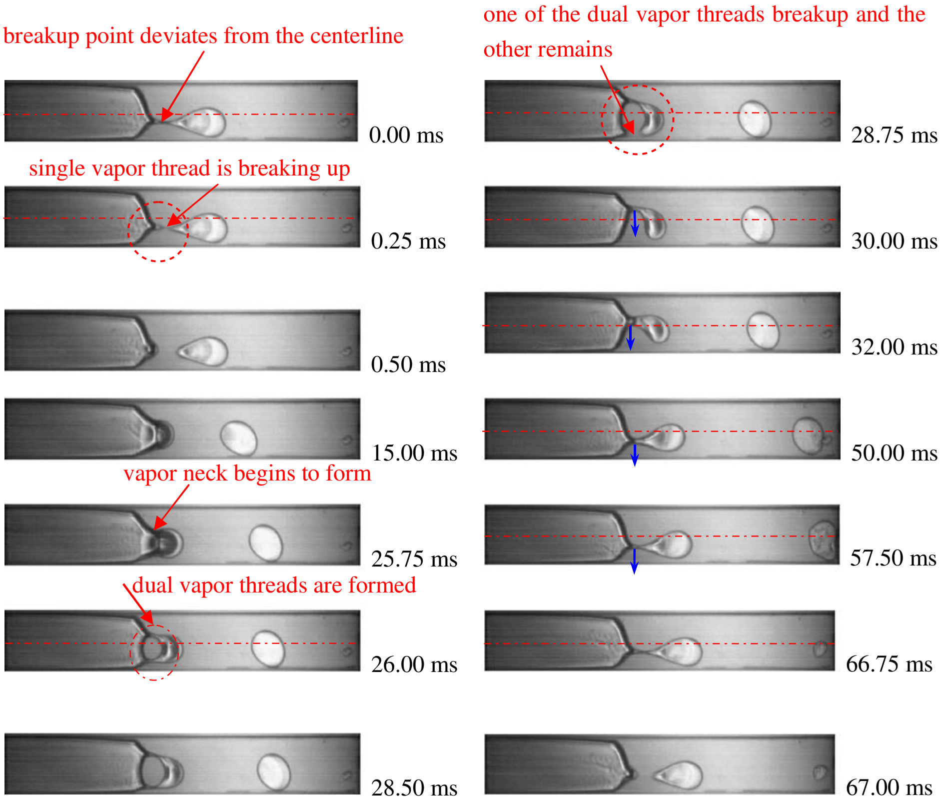

Fig. 8. Miniature bubble formation at the front of elongated bubble in the side channel 1, double vapor thread breakup mode ($p_{in} = 123.12$ kPa, $G = 109.1$ kg/m^2 s).

formation are plotted versus a set of consecutive cycles. In each subfigure of Fig. 11, it is found that cycle periods are larger in the center channel than those in the two side channels, indicating that miniature bubbles are more easily to be separated from the elongated bubble in side channels. In other words, the non-uniform temperature at the etched channel surface leads to the easy miniature bubble formation in side channels. It is interesting to note that the two side channels have nearly the same cycle periods for any cycles.

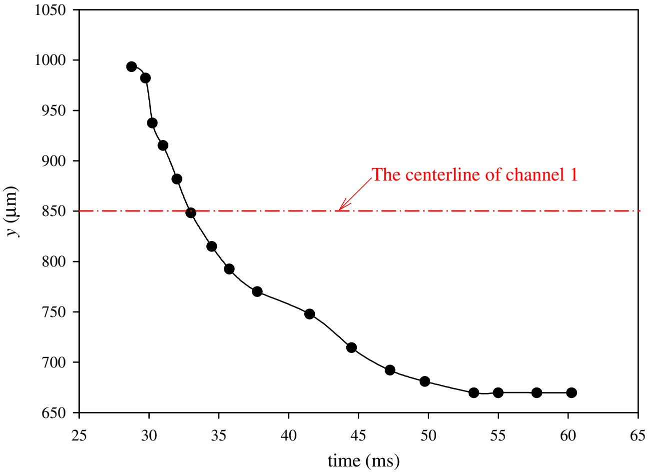

Fig. 9. Migration of the remained vapor thread in *y*-direction, same case as in Fig. 8.

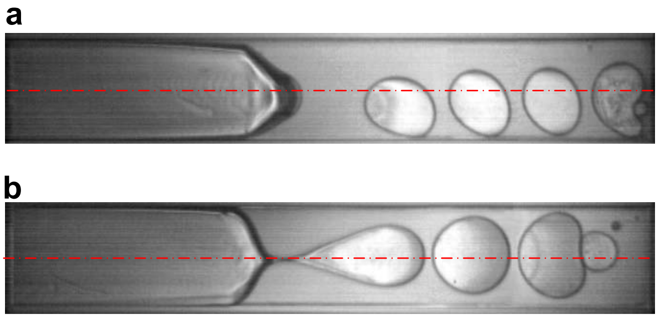

Fig. 10. Bubble trajectory after its departure from the elongated bubble. (a) Side channel 1; (b) center channel 2.

4. Conclusions

We examine the multi-channel effect of the condensation flow in triple microchannels under the air natural convection heat transfer condition. The silicon chip consists of wider and deeper inlet and outlet fluid plenums, and three central parallel rectangular microchannels with the depth down to 30 µm. General flow patterns are either the elongated bubble followed by a detaching or detached miniature bubble at low inlet vapor pressures, or the annular flow at higher inlet vapor pressures. This paper gives a method for generation of miniature bubbles in microchannels for microfluidics applications. It is observed that flow images in the center channel are symmetry against the channel centerline at any time. The miniature bubbles are either separated from the elongated bubble with the single vapor thread breakup mode, or the dual vapor threads breakup mode.

It is found that small temperature variation over the channel width direction affects miniature bubble formation patterns in side channels. The elongate bubble interface is no longer symmetry against the channel centerline. The deviation of the elongated bubble interface tip from the channel centerline is caused by the larger Weber number at that location. The vapor thread and the generating bubble also deviate from the side channel centerline and approach the center channel, due to the Marangoni effect caused by the non-uniform temperature in the width direction of the side channel. The Marangoni effect further makes the miniature bubble contacted with the side wall of the side channels. A shear force coming from the surrounding liquid is applied on the separated miniature bubble along the flow direction. The other force is caused by the Marangoni effect. The combined effect of the two forces switches an inclined bubble position when it is just separated from the elongated bubble to a “standing up” position when it approaches the channel exit. Similar to the bubble generation in the center channel, there are also two miniature bubble generation modes: the single vapor thread breakup mode and the dual vapor threads breakup mode. The side channels have faster miniature bubble generation rates than the center channel, but the two side channels have almost the same miniature bubble generation rates.

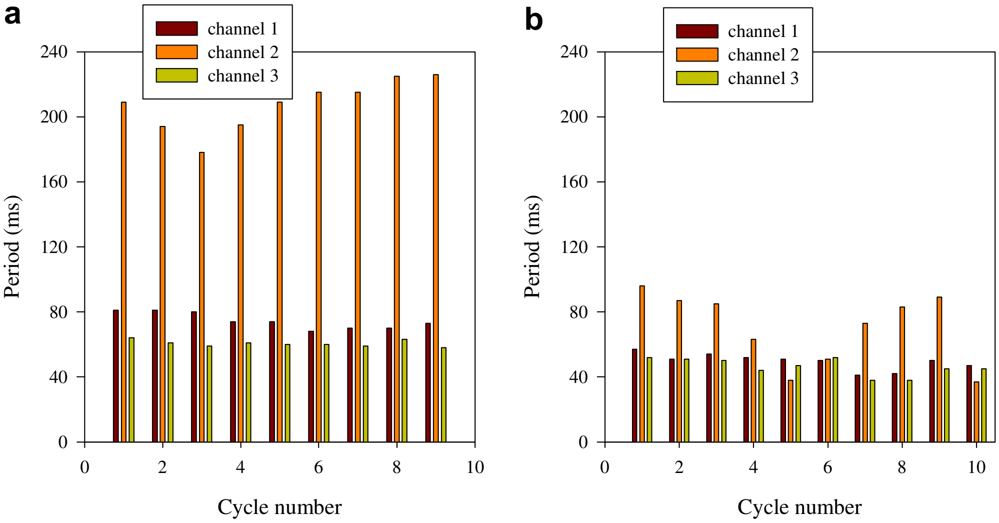

Fig. 11. Miniature bubble generation period for the three microchannels (a) $p_{in} = 123.12$ kPa, $G = 109.1$ kg/m^2 s, (b) $p_{in} = 133.17$ kPa, $G = 123.6$ kg/m^2 s.

Acknowledgments

The authors are thankful for the financial support by the Natural Science Foundation of China (50776089) and the National Basic Research Program (2006CB601203).

References

Baird, J.R., Fletcher, D.F., Haynes, B.S., 2003. Local condensation heat transfer rates in fine passages. Int. J. Heat Mass Transf. 46, 4453–4466.

Médéric, B., Lavieille, P., Miscevic, M., 2005. Void fraction invariance properties of condensation flow inside a capillary glass tube. Int. J. Multiphase Flow 31, 1049–1058.

Shin, J.S., Kim, M.H., 2004. An experimental study of condensation heat transfer inside a mini-channels with a new measurement technique. Int. J. Multiphase Flow 30, 311–325.

Médéric, B., Miscevic, M., Platel, V., Lavieille, P., Joly, J.L., 2004. Experimental study of flow characteristics during condensation in narrow channels: the influence of the diameter channel on structure patterns. Superlattices Microstruct. 35, 573–586.

Wang, H.S., Rose, J.W., Honda, H., 2004. A theoretical model of film condensation in square section horizontal microchannels. Chem. Eng. Res. Des. 82, 430–434.

Wang, H.S., Rose, J.W., 2006. Film condensation in horizontal microchannels: effect of channel shape. Int. J. Therm. Sci. 45, 1205–1212.

Garimella, S., Killion, J.D., Coleman, J.W., 2002. An experimentally validated model for two-phase pressure drop in the intermittent flow regime for circular microchannels. J. Fluids Eng. Trans. ASME 124, 205–214.

Garimella, S., Agarwal, A., Killion, J.D., 2005. Condensation pressure drop in circular microchannels. Heat Transf. Eng. 26, 28–35.

Bandhauer, T.M., Agarwal, A., Garimella, S., 2006. Measurement and modeling of condensation heat transfer coefficients in circular microchannels. J. Heat Transf. Trans. ASME 128, 1050–1059.

Coleman, J.W., Garimella, S., 2002. Two-phase flow regimes in round, square, rectangular tubes during condensation of refrigerant R14a. Int. J. Refrig. 26, 117–128.

Kalman, H., 2003. Condensation of bubbles in miscible liquids. Int. J. Heat Mass Transf. 46, 2451–2463.

Kalman, H., 2006. Condensation of a bubble train in immiscible liquids. Int. J. Heat Mass Transf. 49, 2391–2395.

Louahlia-Gualous, H., Mecheri, B., 2007. Unsteady steam condensation flow pattern inside a miniature tube. Appl. Therm. Eng. 27, 1225–1235.

Wu, H.Y., Cheng, P., 2005. Condensation flow patterns in silicon microchannels. Int. J. Heat Mass Transf. 48, 2186–2197.

Hu, S.J., Chao, C.H.Y., 2007. A experimental study of the fluid flow and heat transfer characteristics in micro-condensers with slug-bubbly flow. Int. J. Refrig. 30, 1309–1318.

Zhang, W., Xu, J.L., Thome, J.R., 2008. Periodic bubble emission and appearance of an ordered bubble sequence(train) during condensation in a single microchannel. Int. J. Heat Mass Transf. 51, 3420–3433.

Stone, H.A., Stroock, A.D., Ajdari, A., 2004. Engineering flows in small devices: microfluidics toward a lab-on-a-chip. Ann. Rev. Fluid Mech. 36, 381–411.

Xu, J.L., Zhang, W., Wang, Q.W., Su, Q.C., 2006. Flow instability and transient flow patterns inside intercrossed microchannel array in a micro time-scale. Int. J. Multiphase Flow 32, 568–592.

Purday, H.F.P., 1949. An Introduction to the Mechanics of Viscous Flow. (Streamline Flow). Dover Publications Inc., New York.

Takahashi, K., Weng, J.G., Tien, C.L., 1999. Marangoni effect in microbubble systems. Microscale Thermophys. Eng. 3, 169–182.